

Octet lattice-based plate for elastic wave control

Giulia Aguzzi^{1,*}, Constantinos Kanellopoulos¹, Richard Wiltshaw², Richard V. Craster^{2,3,4}, Eleni N. Chatzi¹, and Andrea Colombi¹

¹Department of Civil, Environmental and Geomatic Engineering, ETH Zürich, Zürich 8093, Switzerland

²Department of Mathematics, Imperial College London, London SW7 2AZ, United Kingdom

³Department of Mechanical Engineering, Imperial College London, London SW7 2AZ, United Kingdom

⁴UMI 2004 Abraham de Moivre-CNRS, Imperial College London, London SW7 2AZ, United Kingdom

*aguzzi@ibk.baug.ethz.ch

ABSTRACT

Motivated by the importance of lattice structures in multiple fields, we investigate the propagation of flexural waves in a thin woven plate augmented with two classes of metastructures for wave mitigation and guiding, namely metabarriers and metalenses. The cellular architecture of this plate invokes the well-known octet topology, while the metadevices rely on novel customized octets either comprising spherical masses added to the midpoint of their struts or variable node thickness.

We numerically determine the dispersion curves of a doubly-periodic array of octets, which produce a broad bandgap whose underlying physics is elucidated and leveraged as a design paradigm, allowing the construction of a metabarrier effective for inhibiting the transmission of waves. More sophisticated effects emerge upon parametric analyses of the added masses and node thickness, leading to graded designs that spatially filter waves through an enlarged bandgap via rainbow trapping. Additionally, Luneburg and Maxwell metalenses are realized using the spatial modulation of the tuning parameters and numerically tested. Wavefronts impinging on these structures are progressively curved within the inhomogeneous media and steered toward a focal point. Our results yield new perspectives for the use of octet-like lattices, paving the way for promising applications in vibration isolation and energy focusing.

Introduction

Lattice materials are engineered periodic structures whose cellular architecture originates from a network of entangled structural elements (e.g., rods, beams, or plates)¹. Their high strength-to-weight ratio, combined with recent progress in additive manufacturing, renders them particularly attractive for the scientific community; their unique mechanical performance has been extensively explored², with broad application in biomedicine, aerospace and energy absorption. It is only recently that these have drawn attention for their ability to diffract waves and behave as filters³ that forbid energy transmission across selected frequencies, known as *bandgaps*⁴. The periodic nature of these reticulated structures is often at the root of their attenuation mechanism, leading to Bragg scattering effects⁵ that dominate the spectrum of their band structure⁶. Bragg bandgaps arise through destructive interference, occurring when the wavelength of a wave is comparable to the fundamental period of the media they are propagating through, and typically occur at frequencies too high to be exploited. Much work has been done to broaden Bragg bandgaps by introducing locally resonant objects, whose resonance coincides with the Bragg frequency⁷⁻⁹, wherein lattice vectors are carefully chosen such that these frequencies coincide.

Despite offering wave control, Bragg-based frame designs suffer from a periodicity requirement that forces their characteristic size to comply with the targeted wavelength⁴ thus, limiting their role. To overcome this limitation, attempts are being made to design lattices with resonance-induced bandgaps that, unlike their phononic counterpart, exploit the coupling between propagating waves and resonating components and offer greater tuning flexibility at subwavelength scale (i.e., the size of the unit cell can be orders of magnitude smaller than the wavelength). These structures form a subset of *single-phase metamaterials*¹⁰⁻¹² that use auxiliary resonators or inborn resonant modes of the lattice to hybridize propagating waves and inhibit their transmission. Common practice for their implementation includes, for instance, embedding stand-alone resonant elements (e.g., cantilever beams¹⁰) into an original frame-based topology, similarly to the solution proposed by Li *et al.*¹³ A different method, adopted by An *et al.* in¹⁴ uses, instead, the constitutive matrix of a body-centered cubic (BCC) lattice and constructs an integrated resonator via radius jump of its strut cross-section. The BCC cell is only one of the Bravais lattices^{5,15} potentially serving as metamaterials. Among the fourteen types known to exist in the three-dimensional space⁵, the *octet* design¹⁶ is an example of face-centered cubic (FCC) topology with promising attenuation potential. The dispersive behavior of this lattice, already renowned in statics for its high strength combined with a slender lightweight profile¹⁷, has been outlined by Arya *et al.*¹⁸ who show that the octet supports a bandgap whose existence depends upon the aspect ratio of the struts, but do not investigate the underlying physics of its generating mechanism; only briefly suggested by Gerard *et al.*¹⁹. In addition,

most of the state-of-the-art research on such a FCC cell resort to frequency gaps produced by attached resonators¹² or use it as a constitutive matrix of multi-phased materials^{20,21}, without delving into its inherent resonant modes. The absence of an overarching dynamic assessment of this architecture in the existing literature emphasizes the novelty of our work, which proposes the octet topology as a metamaterial lattice endowed with an energy gap stemming from the bending local resonance of its beam-like members. Moreover, due to the arrangement and behavior of wave propagation through the struts, we show that the octet cells form a medium in which flexural resonances naturally coincide with the Bragg frequency - as observed within the eigenmodes permitted by Floquet-Bloch waves.

In aerospace and aircraft engineering, lattice plates are frequently used as structural components or filling in sandwich panels¹ that, whilst providing lightness to the structure², are liable to significant vibrations. The propagation of such vibrations in solid thin plates, occurring in the form of Lamb waves with different polarization, has been extensively documented^{22,23} resulting in a variety of metamaterial-based solutions. Prominent among these are *metabarriers* (or *metawedges*²⁴) encompassing clusters of rods whose longitudinal resonant mode couples with the flexural waves propagating in the plate and triggers the opening of bandgaps^{25,26}. To enlarge the frequency band of such barriers, that owing to local resonance offer a fairly limited range of applicability, *graded* designs have been explored, where the spatial variation of the tuning parameter, rod height, yields a wider spectrum of attenuation associated to the so-called Rainbow trapping effect^{27,28}. The theory underpinning these metastructures can be easily applied to octet-based plates, with the longitudinal resonances replaced by the bending mode of the struts and the rod height by the parameters of the beam-like members. Based on these considerations, a number of parameters exist in the literature to tune the resonance-bandgap, two of which are of particular interest for the present study, namely auxiliary point masses and joint stiffness. Junyi *et al.*¹² proposed equipping the end of cantilever beams, added to primary 3D Bravais lattices, with point masses whose size governs the gap frequency independently of the geometry of the base lattice. Shortly before this, the same spherical masses were attached to the joints of a Kagome lattice by Liu *et al.*²⁹ to stiffen its connections and open a bandgap tied to the rod-node vibration.

Beyond widening the bandgaps, graded designs lay the foundation for a multitude of compelling wave control possibilities. One of these dates back to the nineteenth century and the seminal work of Maxwell on so-called flat or *gradient-index (GRIN) lenses*³⁰. These are effective, aberration-free devices that leverage composite structures to adjust the spatial distribution of the refractive index within a bounded region and ultimately shape the incident wavefronts. The *Luneburg lens*³¹ is a type of spherical GRIN lens that diverts any collimated beam colliding at its boundaries to a diametrically opposite focal point. Similarly to this system, underpinned by a refractive index that increases radially from the outer toward the center of the graded area, the *Maxwell fish-eye lens*, bends the trajectories of rays originated by a point source at its surface and focuses them in a mirrored image point. While building such lenses with ordinary composite materials appears a daunting task, employing phononic crystals^{32,33} or metamaterials^{34,35} considerably relieves this complexity. From a metamaterial perspective, the cluster of locally resonant rods with graded height, previously discussed, has proven an effective candidate for the design of GRIN lenses³⁶⁻³⁸. Its rod-resonance bandgap, besides providing attenuation, serves as tuning variable for the phase velocity of waves traveling in the metastructure and leads to applications at different scales, from acoustics³⁶ to seismology³⁹. In terms of frame structures, the research on wave guiding is still at a primordial state, mainly confined to two-dimensional lattices⁴⁰⁻⁴³ and yielding, only in a handful of cases, to more sophisticated effects. Xie *et al.*⁴⁴ and Zhao *et al.*⁴⁵ were among the few to design 2D and 3D flattened Luneburg lenses consisting of a three-dimensional truss-based square lattice, to manipulate waves in the ultrasound regime. A recent study⁴⁶, on the other hand, has explored the propagation of elastic waves in three-dimensional lattices, including specifically the octet cell. Although similar to our investigation with respect to the choice of topology, no bandgap is reported in this case and only the anisotropic character of the structure is emphasized, with no explicit reference to shaping wave trajectories via graded octet lattices. Therefore, the lack of existing literature on gradient-index lenses designed with octet lattices further motivates our work.

Here we take the octet lattice analysis one step further by using this geometry to realize a reticulated plate and two types of integrated devices for flexural wave mitigation and control. Following a dispersion analysis of the proposed standard octet cell, the bandgap and its underlying generation mechanism are revealed, resulting in the identification of two tailoring parameters. Auxiliary masses, embedded in the midpoint of the struts, or variable joint thickness are used to tune the frequency range with forbidden propagation as well as the phase velocity spatially within the lattice. To avoid redundancy of results, only those stemming from the addition of masses to the primary cell are reported here; varying the node thickness produces similar outcomes. Two metabarrier designs are discussed, the first characterized by constant auxiliary masses and the second relying on the grading strategy to trap and hinder wave transmission over a wider frequency band. Finally, Luneburg and Maxwell lenses are built by smoothly increasing the supplementary spherical masses radially from the boundaries to the center of the devices. We find the octet cell and subsequent customizations possess desirable dispersive properties easily coaxed to required frequencies, these properties are readily exploited to create a variety of devices able to manipulate the propagation of waves over a variety of scales, in both a subwavelength (lenses) and Bragg (metabarriers) scattering regime.

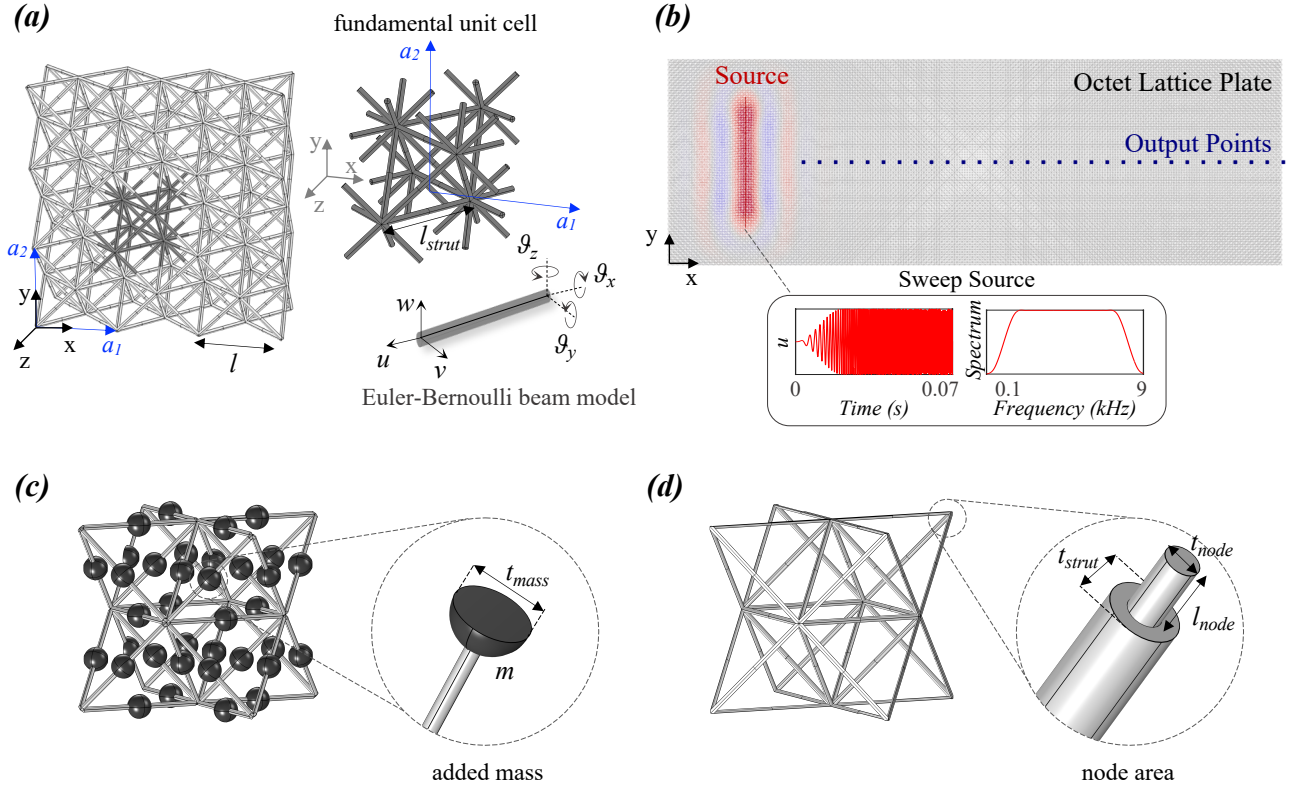


Figure 1. Cell designs and setups for dispersion and parametric analyses. (a) 2D standard octet lattice with fundamental unit cell depicted in the zoom ($\mathbf{a}_1 = (l, 0, 0)$ and $\mathbf{a}_2 = (0, l, 0)$). (b) Finite lattice plate ($3.6 \times 1.2 \times 0.03$ m) for the validation of the band structure via time-transient simulations in Real-ESSI. The constitutive unit corresponds to the standard octet reported in (a). The plane sweep source and line of points where the output signal is recorded, spaced 0.03 m apart and located on the nodes of the lattice, are marked in red and blue. (c) Customized octet equipped with spherical masses m , of diameter t_{mass} , (dark color) added to the midpoint of the struts. (d) Octet with customized joints via tunable node thickness, t_{node} . The zoomed plot inset shows the node area of length l_{node} equal to $2l_{strut}$ and of variable thickness t_{node} .

Results

Octet cell design, dispersion and parametric analyses

Consider a thin reticulated plate, of infinite extension, constructed from repeating unit cells, each comprising a strut network generating the well-known octet topology¹⁶. We choose a fundamental cell whose edges coincide with the midpoint of the octet struts, as depicted in Figure 1a, where we define physical basis vectors \mathbf{a}_1 and \mathbf{a}_2 , assumed collinear with the Cartesian axes x and y . We consider struts of circular cross-section, of diameter $t_{strut} = 1$ mm, Young's modulus $E = 1.7$ GPa, density $\rho = 450$ kg/m³ and Poisson's ratio $\nu = 0.3$. We take the length of our lattice vectors to be $l = 3$ cm and hence have a strut length of $l_{strut} = l\sqrt{2}/2$. The circular cross-section provides axial symmetry and prevents stress concentration that would instead arise in sharp-edged profiles, e.g., square cross-section.

It is sufficient to consider waves propagating through the fundamental cell as the phase shift from cell-to-cell is completely described by the dispersion relation between eigenfrequencies and Bloch-wavevector, corresponding to the red dotted line reported in Figure 2a (see Methods). Despite the complexity of this folded band structure, three main frequency bands can be clearly identified.

In the low-frequency limit, from 0 to 2 kHz, the spectrum is dominated by zero-order modes similar to the solutions of Lamb's characteristic equations in solid, homogeneous, and thin plates for long wavelengths²². The underlying lattice structure has subwavelength behavior and wave propagation closely resembles an equivalent continuum supporting three propagating waves, respectively two with transverse and one with longitudinal polarization⁴⁷. Among these, the asymmetric flexural mode, simply denoted as A_0 mode in Figure 2a, is the most attractive for its ease of activation and amount of carried energy hence, the cornerstone of this study.

At higher frequencies (2 to 5 kHz), the wavelength reduces rapidly and waves interacting with the detailed geometry of the cell open a *bandgap* between 3.85 and 5.08 kHz. Waves with frequency content matching this range are prevented from penetrating the octet lattice while being trapped by the bending vibrations of its struts. These deformations emerge as flat bands in the lower bound of the forbidden interval and serve as evidence of its local resonance-based generating mechanism⁴⁸. They

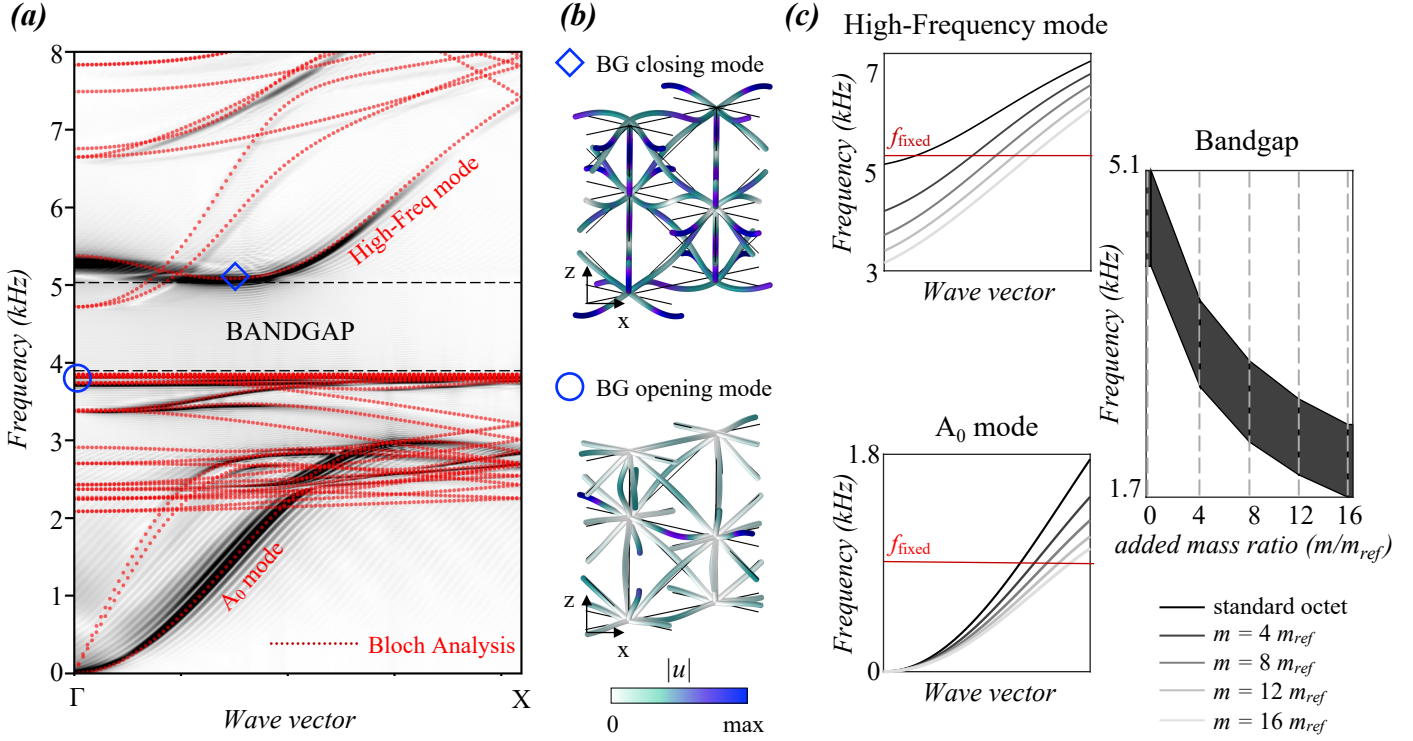


Figure 2. Dispersion analysis. (a) Band structures of the standard octet crystal and finite plate (Figures 1a, b) computed with Comsol Multiphysics (red) and Real-ESSI (black). The Γ -X wavevector in the reciprocal space represents waves propagating in the \mathbf{e}_x direction in the physical system. The red curves are obtained via Bloch-eigenvalue analysis on the fundamental unit cell of Figure 1a. The black branches derive from the fast Fourier transform (FFT) of the z -wise signal recorded on the receivers of Figure 1b, where they are denoted as output points and colored in blue. (b) Bandgap (BG) opening and closing eigenmodes, respectively at 3.85 and 5.08 kHz. (c) Sensitivity analysis on the dispersion curves of the customized octet cell (Figure 1c) for increasing m , where $m_{ref} = \rho A 2l_{strut}$.

cluster around the first flexural frequency of a clamped-clamped Euler-Bernoulli (EB) beam, geometrically equivalent to the struts in the octet and defined by:

$$f_{clamped} = \frac{22.4}{2\pi l_{strut}^2} \sqrt{\frac{EI}{\rho A}} \quad (1)$$

The analytical flexural frequency in Equation (1), equal to 3.85 kHz, corresponds to the bandgap opening bound and poses as a design variable for tailoring the bandgap frequency range. By considering the octet struts as equivalent EB beams with clamped edges and bending resonance¹¹, the bandgap opening frequency can be estimated via Equation (1) and, consequently, also the correlated attenuation zone⁴⁹. This simplification reduces the complexity of the octet cell to individual beams clamped at the nodes, facilitating the tuning of design parameters. This clamped-clamped nodal behavior relies on a network of highly connected struts peculiar of the octet topology. As outlined in Wang *et al.*⁴⁹ highly connected lattices (here intersection points of 12 members at a node) yield a clamped-clamped behavior of the struts at the nodes. Similarly to Nolde *et al.*⁵⁰, our flat bands at $f_{clamped}$ correspond to standing waves induced by the fundamental resonance of vibrations along clamped-clamped beams. This behavior is highlighted in the BG opening eigenmode displayed in Figure 2b, where the nodes stand still. Furthermore, such a fundamental resonance fits exactly within the length of the primitive lattice vectors (a half our conventional unit cell), hence the propagation regime is identical to Kaina *et al.*⁷ in which the wavelength of the fundamental clamped-clamped resonance is twice that of the modulus of the primitive lattice vectors; subsequently the Bragg frequency and $f_{clamped}$ coalesce, resulting in destructive interferences producing a broad bandgap. Wang *et al.*⁴⁹ remarks that bandgaps, in this setting, are generated by local resonances and not Bragg scattering; however, in the case where beams are parallel to and of the same length as the primitive lattice vectors, one expects a medium in which the fundamental resonances naturally match the Bragg frequencies, all of which are properties the underlying octet cell possesses.

Beyond the bandgap, approximately from 5 to 8 kHz, additional dispersive modes populate the spectrum of the dispersion relation, mimicking waves that propagate at the strut level accompanied by roto-translations of the nodes. In particular, a branch with predominant orientation along z , denoted as *high-frequency mode* in Figure 2a, can be observed. Owing to its polarization,

this defines the upper bound of the attenuation zone (see top inset in Figure 2b), in contrast to the two modes converging at 4.7 kHz, which exhibit, instead, in-plane deformations.

One known limitation of the Bloch analysis is that only a minority of the computed modes are triggered owing to their strong source dependence. Hence, a finite octet-based plate, consisting of 120 x 40 cells equivalent to the one of the infinite study (Figure 1b), is adopted to corroborate the predicted band structure via time-domain simulations (see Methods). The outcome of this analysis is shown as a background of the dispersion curves in Figure 2a, where the branches involving out-of-plane deformations are predominantly excited. Almost complete superposition can be appreciated between the A_0 and high-frequency modes of the frequency-wavenumber spectrum and that of the Bloch analysis. A small discrepancy arises only in the higher-order modes and in the upper bound of the bandgap, with a downward shift of about 0.05 kHz in the results of the time-transient simulation. From 2 to 4 kHz, additional modes, generated by waves with polarization in the lattice plane (longitudinal or shear), are effectively captured by the finite model. Overall, the results of these two types of analyses reveal good agreement and justify their joint application in the following sections.

The octet unit outlined hitherto, comprising 24 woven struts of constant, circular cross-section, is denoted as the *standard cell*. Remarkably, a local resonance-induced bandgap originates in this single-block lattice owing to the refined topology of its design, thus paving the way for a variety of parameters to be leveraged in tuning the dispersion relations. While geometrical and material properties emerge as the primary natural candidate, their influence on the octet band structure has already been assessed^{18,51}. The focus here shifts to two novel, so-called, *customized octet cells* whose parameters allow tailoring the band structure without affecting the original geometry, i.e., cell width and strut thickness. In the customized cell of Figure 1c the midpoint of the struts is endowed with auxiliary spherical masses, m , of diameter t_{mass} , as this undergoes major displacements when bending deformations are activated. In order to retain a monolithic structure, easier to 3D print with modern techniques, the supplementary mass is made of the same material selected for the lattice and is expressed as a multiple of a reference value, $m_{ref} = \rho A 2 t_{strut}$. The diameter t_{mass} in Figure 1c is then derived upon definition of this quantity and its practical feasibility, with respect to the thickness of the struts, is adequately verified in each of the proposed devices. The spheres are added as point masses in the finite element model in Comsol 5.6 and the sensitivity analysis is performed on the single customized unit via Bloch theory. Likewise the approach adopted for the standard octet cell, the struts are treated as equivalent fixed-fixed Euler-Bernoulli beams with the distributed mass, $\rho A l_{strut}$, incremented by the point mass m . Naturally one expects these added masses to provide a damping over the whole band structure reducing the frequencies of comparable eigenmodes, as observed in Figure 5b. The first fundamental frequency, governing the position of the bandgap, has an inverse reliance on the added mass, as already analytically proven by Low *et al.*⁵². When m increases, the bandgap is instantly shifted to lower frequencies, from the range 3.85-5.08 kHz to 1.73-2.74 kHz in the rightmost inset of Figure 2c, altering the A_0 and high-frequency modes. Each point in these dispersion curves has an associated phase velocity, $v_p = \omega/k_x$ ⁵, which decreases when moving from lighter to heavier masses at constant frequency (red line in Figure 2c), thereby animating the lattice with slower waves. Similar outcomes arise when exploring the customized cell in Figure 1d. Following the analogy between octet struts and clamped EB beams, we harness the topology of the connections in the lattice to modify the boundary conditions of the equivalent beams and their natural resonant frequency, in turn affecting the band structure of the architected cell. A node area of length l_{node} , twice as long as t_{strut} , is identified in Figure 1d, where the diameter of the section, t_{node} , is expressed as a fraction of the original thickness t_{strut} . By decreasing this parameter from t_{strut} to $0.2t_{strut}$, clamped-like joints are replaced by quasi-hinged connections that allow almost free rotations between contiguous struts. This yields a substantial reduction of the node bending stiffness, which is proportional to the moment of inertia, I , and consequently to the joint thickness, t_{strut}^4 . The bandgap opening frequency is therefore shifted from the value reported in Equation (1) to that of a simply supported beam, $f_{pinned} = 0.44f_{clamped}$, entailing a slope-related change in the low (A_0) and high-frequency branches. Again, the phase velocity of the waves diminishes, leading to slower waves propagating in the hinge-like octet lattice and faster waves being instead transmitted by the stiffer, clamped-based frames.

In designing the cell of Figure 1d, compliant joints were preferred over decoupling the struts with prefabricated hinge-connectors as they preserve the single-phase material while allowing a gradually varying stiffness of the connections. Although beyond the scope of this study, it is important to point out that this choice may cause a high stress concentration in the joints that must be examined prior to fabrication.

Wave propagation in finite meta-lattices

The computational domain, depicted in Figure 3a, is a 3 cm thick reticulated plate assembled by spatially tessellating the standard octet cell illustrated in Figure 1a. A so-called *meta-area* lies within this structure, where the parameters of the octet, introduced in the previous Section and expressed in terms of supplementary masses or joint stiffness, are progressively tuned to yield exotic attenuation or wave guiding phenomena. Therefore, two types of devices are built, as reported in Figures 3b and c: the *metabarriers* and *metalenses*. The metabarriers leverage an arrangement of customized octet units, either tailored at the same or diverse frequencies, to generate an inhibited frequency range, where the displacement field vanishes and ultimately

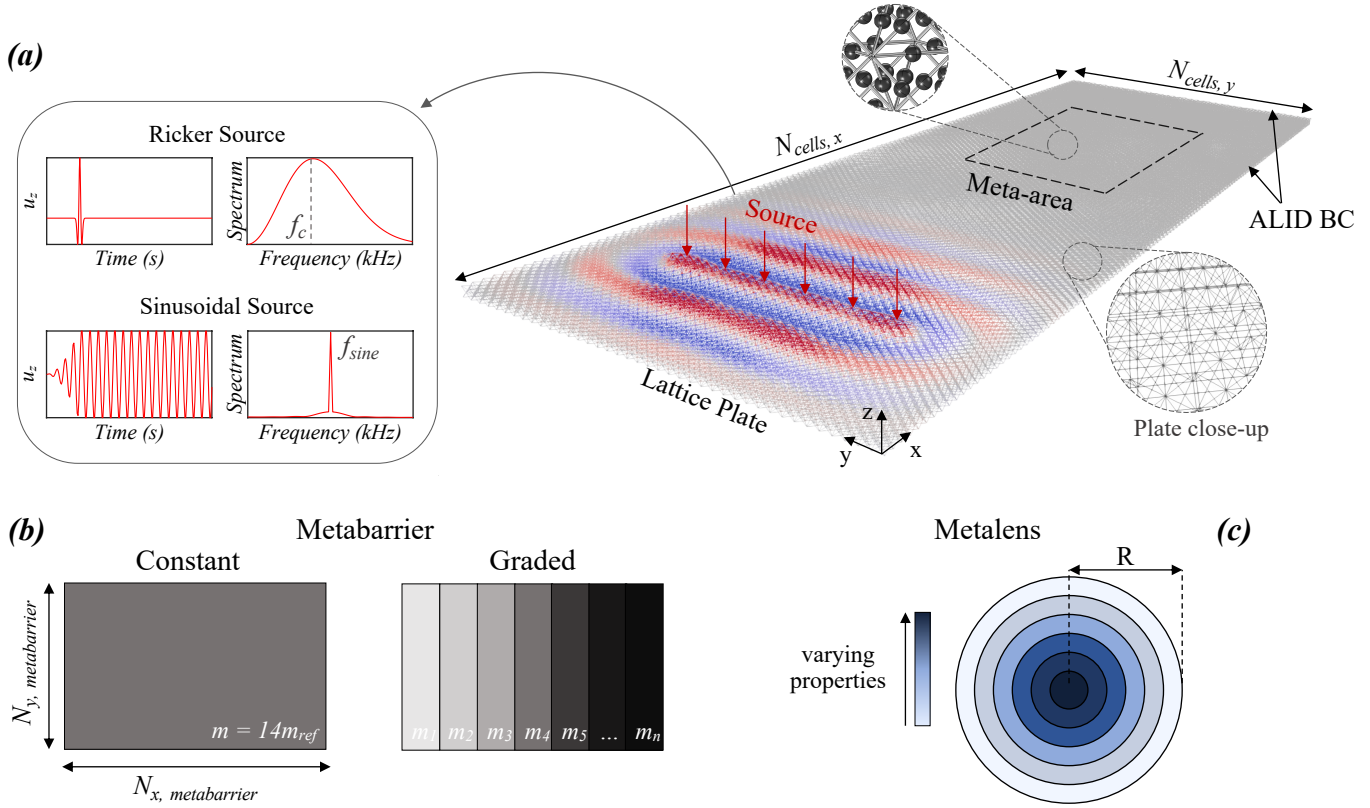


Figure 3. Setup for time-transient simulations in Real-ESSI. (a) Lattice plate made of standard octet units as detailed by the close-up. The meta-area (dashed black line) consists of embedded-mass octets arranged as rectangular metabarriers or circular metalenses, as reported in (b) and (c). Absorbing boundary conditions with quadratically increasing damping⁵³ (ALID) are implemented on all four edges of the plate. The two sources used for the metabarriers (Ricker) and metalenses (sine) are sketched in the inset. (b) Metabarriers of customized cells with auxiliary masses. On the left side, the constant setup (50×20) encloses cells with $m = 14m_{ref}$. The graded configuration is formed by 30×20 cells of progressively increasing masses, m_n with $n = 1, \dots, 15$. Each layer comprises two rows of octet cells with identical supplementary mass. (c) Layout for Luneburg and Maxwell metalenses featuring concentric circular layers with variable point masses. In both cases, the lens radius, R , consists of 12 cells of width l and the source is a sinusoidal excitation tuned at the design frequency of the lens.

shield a target area. Conversely, the metalens relies upon the spatial variation of lattice properties to modify the refractive index in an inhomogeneous bounded region and manipulate wave trajectories, eventually offering the opportunity to focus and harvest vibration energy.

Wave propagation in lattice metabarriers

Two lattice metabarriers, comprising mass-embedded octets, are implemented within a lattice plate made of 120 by 40 standard cells, arranged as per the configuration in Figure 3a, and separately investigated in this section.

Illustrated in Figure 3b is the 50×20 cells *constant metabarrier*, where the struts of the octets are equipped with midpoint masses, m , equal to $14m_{ref}$ ($t_{mass} = 3.5$ mm), yielding an attenuation zone from 1.8 to 2.8 kHz (gray region in Figure 4d). The metastructure is assessed under excitation of a 60ms Ricker wavelet located at a distance of 45 cells to guarantee a plane wavefront. The spectrum of the source, with dominant component along z , is centered on the bandgap, at 2.1 kHz.

The recorded displacement field u_z , filtered inside the bandgap at two sequential instants in Figures 4a and c (see video in the Supplementary Material), unveils the attenuation potential of the lattice metabarrier, based on Fano-like resonances⁵⁴. At $t = 7.2$ ms, the flexural waves scattered by the resonating mass-struts in the metawedge interfere destructively with the unscattered incoming field, impeding the transmission of energy⁵⁵. The resulting energy gap, originated by the hybridization between the asymmetric propagating Lamb wave and the coalescence of the resonant bending mode of the struts and Bragg scattering, induces splitting of the incident wavefront⁵⁶, as depicted in Figures 4a, c.

This mitigation mechanism, already introduced in the previous Section, is further corroborated by the spectrum of two waveforms, r_1 and r_2 in Figures 4a, b, located on the masses of a cell belonging to the first row of the metabarrier. The signal of the leftmost mass-strut (blue line in Figure 4b) exhibits a pronounced Lorentzian symmetric peak centered at the resonant frequency f_r (1.8 kHz), whilst the second waveform, r_2 , reveals the typical asymmetric profile, where a sharp enhancement of the spectrum prior to f_r is followed by a transmission drop (antiresonance)⁵⁴. This Fano-type interference, limited to a narrow

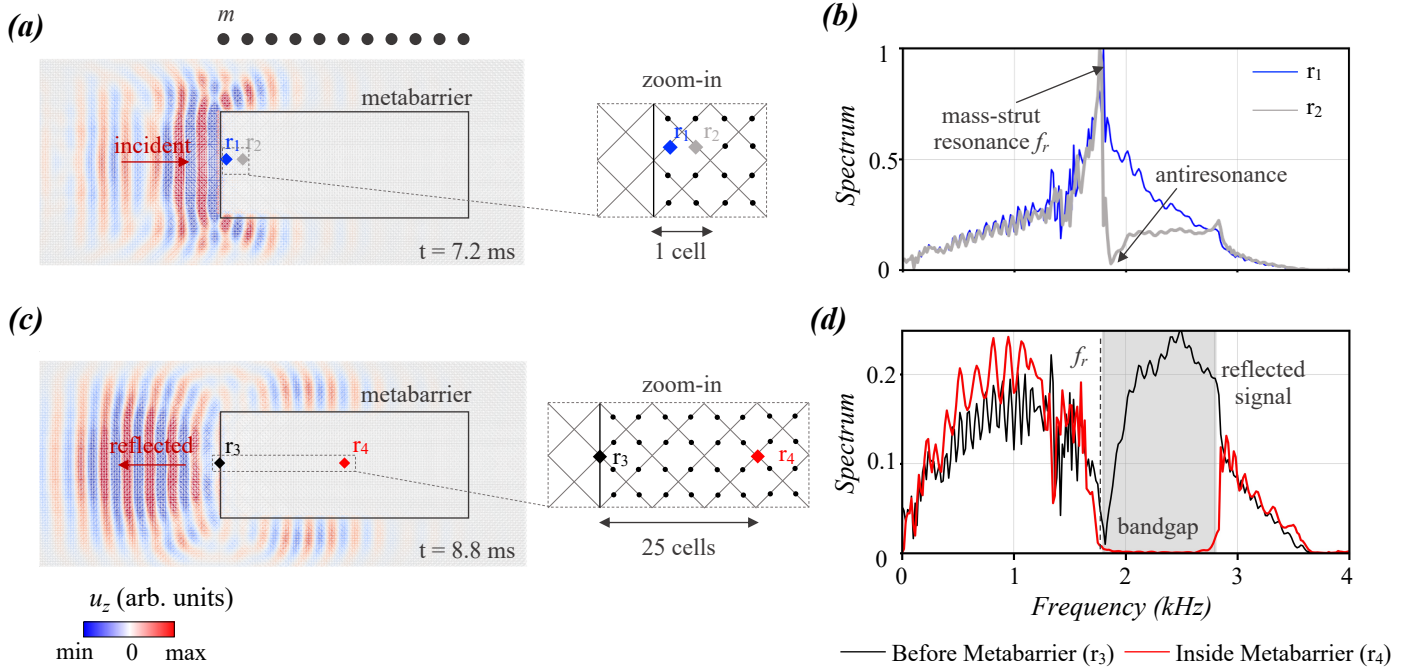


Figure 4. Temporal and spectral wave fields of the constant metabarrier. (a) Propagating Lamb waves filtered within the bandgap (1.8 - 2.8 kHz). The output signal is recorded in two points, r_1 and r_2 , arranged on the midpoint of the struts atop the embedded masses in order to validate the hypothesis of hybridization bandgap. Their spectrum is reported in (b). (c) Filtered displacement field at a later time instant. The back propagating, reflected wavefront is emphasized by the red arrow. Two receivers, located respectively before and within the barrier, are shown in the zoom. Their spectra are compared in (d), after normalization with the peak value of (b).

bandwidth if only the first line of cells in the metabarrier is considered, intensifies when leveraging an array of octets tuned all at the same resonant frequency. By inspecting the spectral displacement of a point located at the core of the metabarrier, after 25 cells (r_4), this effect becomes evident. The resonances of the mass-equipped struts interact constructively yielding a wider attenuation zone that extends from f_r to their antiresonance⁵⁷, as reported by the gray region and red signal in Figure 4d. Furthermore, by comparing this spectrum with the displacement field in a receiver on the edge of the metastructure (r_3), black line in Figure 4d, we observe that the majority of the energy with frequency content within the forbidden range is converted into reflections⁵⁶. The wavefront impacting on the metabarrier at 7.2 ms, propagates backward in the plate at $t=8.8$ ms (Figure 4c) after interacting with the resonating members.

Although effectively hampering wave transmission within the bandgap, the constant metawedge exhibits a fixed frequency range of application stemming from the resonant nature of the attenuation zone that, whilst broadband and easily tuneable, entails spatially localized phenomenon. A mitigation device, equipped with smoothly increasing masses, is designed in order to overcome this drawback, as these were proven to affect the frequency content of the prohibited range (see Figure 2c). The *graded metabarrier*, with masses m_1 to m_{15} ranging from $3m_{ref}$ to $42m_{ref}$, respectively with t_{mass} from 2 to 5 mm, is depicted in the right inset of Figure 3b and tested with an input Ricker source centered at 3 kHz. Following the inverse relationship between added mass and resonant frequency, the heaviest masses (m_{15}) govern the opening frequency of the total bandgap, while the upper bound depends upon the choice of m_1 (see Figure 5b). The evolution of the bandgap is also shown in Figure 5b and reveals how the frequencies within the bandgap decrease spatially as masses increase from grade to grade; waves of a certain frequency propagate through the medium until they reach the spatial location where they exist within a bandgap, at this point they are subsequently trapped and back reflected thus, spatially distilling the spectrum following the Rainbow trapping effect^{24,27,58}. As a result, our medium possesses a wider stop band, from 1.14 kHz to approximately 5.1 kHz (see gray region in Figure 5c).

Figure 5a illustrates the displacement field filtered over two distinct frequency ranges (see videos in the Supplementary Material). Between 1.8 and 2.5 kHz, the wave impinging the metabarrier is almost immediately trapped and scattered by the cells with masses equal to $11m_{ref}$, owing to the matching with their frequency gap (1.98-3.09 kHz). Similarly, the lower frequency field, corresponding to a pass-band filter between 1.2 and 1.5 kHz, travels undisturbed deeper in the metastructure until it eventually interacts with the cells of mass $31m_{ref}$ (bottom inset), the exact location these frequencies occur within the varying bandgap.

As validation, the spectral displacement of a point at the right end of the metawedge is compared to that of a receiver

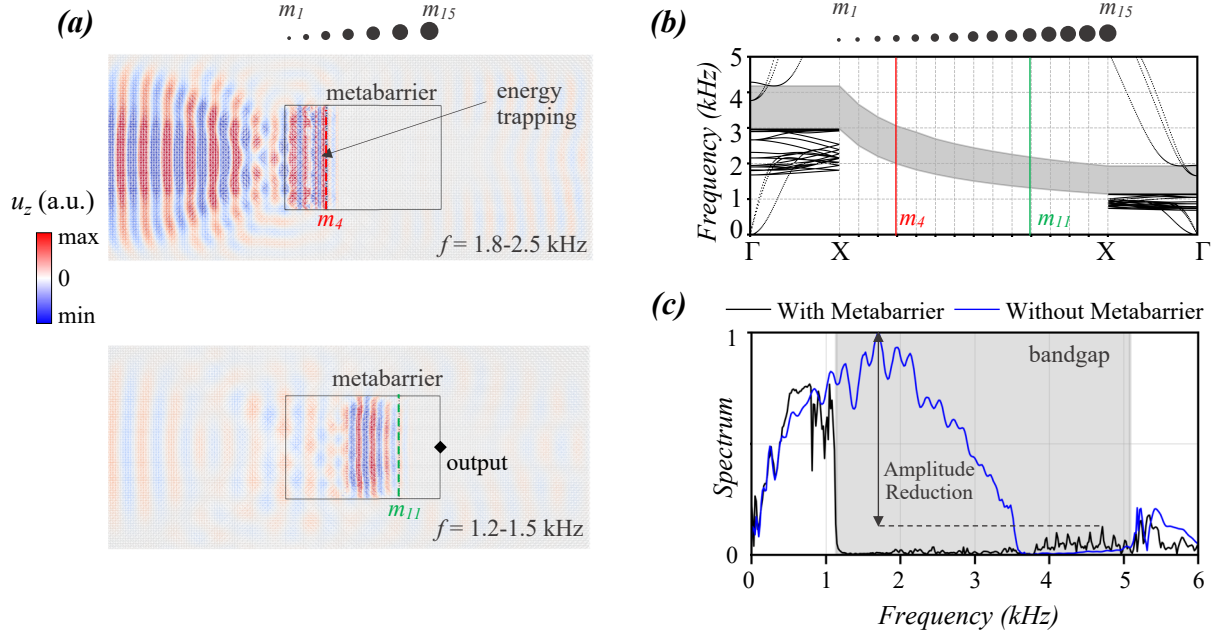


Figure 5. Temporal and spectral wave fields of the graded metabarrier. (a) The top and bottom insets show the displacement field filtered within the bandgaps induced by octets with masses $m_4 = 11m_{ref}$ (red) and $m_{11} = 31m_{ref}$ (green). (b) Evolution of the bandgap within the graded metabarrier, for masses increasing from m_1 to m_{15} , computed via Bloch analysis (see Methods). (c) The spectrum of a signal recorded on the right end of the metabarrier (black), in the output point emphasized in (a), is compared with that of a receiver located at the same position in a bare lattice plate (blue). The bandgap generated by this graded design is highlighted in gray. The amplitude reduction within the bandgap is estimated as the difference between the maximum spectrum of the two signals in the attenuation zone, as illustrated in the figure.

at an equivalent position in a bare lattice plate in Figure 5c. The amplitude reduction, stemming from the presence of the metawedge and approximately equal to 87%, is visibly appreciable, as well as the widening of the bandgap compared to that in Figure 4d. Notice that, a zero-transmission range exists in both the spectra between 3.8 and 5.1 kHz, which can be attributed to the dispersive behavior of the standard octet cells. While being progressively slowed down within the graded barrier, the impinging energy is trapped by the bending resonant mode of the mass-strut in the octets and consequently amplified. Despite seemingly counterproductive, this dynamic behavior underpins an effective broadband device, where wave attenuation and energy harvesting can coexist.

Octet-based gradient index lenses

Drawing from the dynamic properties of the octet lattice, two of the most popular GRIN lenses are engineered from this architecture to shape ray trajectories and focus wave energy. The design of these devices relies on the dependency of the phase velocity, extracted from the dispersion relations, upon the frequency and the tuning parameters. By combining this relationship with the refractive index profile, the design variables of the customized octet cells are derived at different locations in the lens.

Specifically, the Luneburg and Maxwell lenses are created by gradually varying the supplementary masses embedded in the octets, or the stiffness of their joints, designed to produce the required refractive index profile within a bounded region of radius R , which corresponds to 12 cell layers, each featured by a distinct parameter value (Figure 3c). The required theoretical refractive index profile is defined as a function of the radial coordinate, r , centred in the middle of the lens, as follows:

$$n_{Luneburg} = \sqrt{2 - (r/R)^2} \quad \text{and} \quad n_{Maxwell} = 2/(1 + (r/R)^2) \quad (2)$$

The effective wavespeeds in the metalenses, v_{eff} , and in the surrounding lattice plate comprising only standard octets, v_0 , are retrieved from the band structure of the cells, computed via Bloch analysis, with the relationship $v_{eff} = \omega/k$. In order to eliminate their frequency dependence, originated by the dispersive nature of the octet, these quantities are evaluated at fixed components, f_{fix} . The frequencies are selected sufficiently far from the stop band, so as to prevent the waves from being localized and amplified by the strut resonances. At 1 kHz and 5.2 kHz, respectively for the Luneburg ($f_{fix,L}$) and Maxwell ($f_{fix,M}$) lens, the phase velocity is calculated for increasing added masses or node thickness and plotted in the top inset of Figures 6b and c. While both wavespeeds feature a decreasing trend for heavier masses, a significant drop can be observed in the high-frequency branch ($f_{fix,M}$), posing as a suitable candidate for the design of a Maxwell lens, which requires an abrupt variation of the refractive index. The opposite behavior is instead noted when varying the thickness of the nodes yielding a

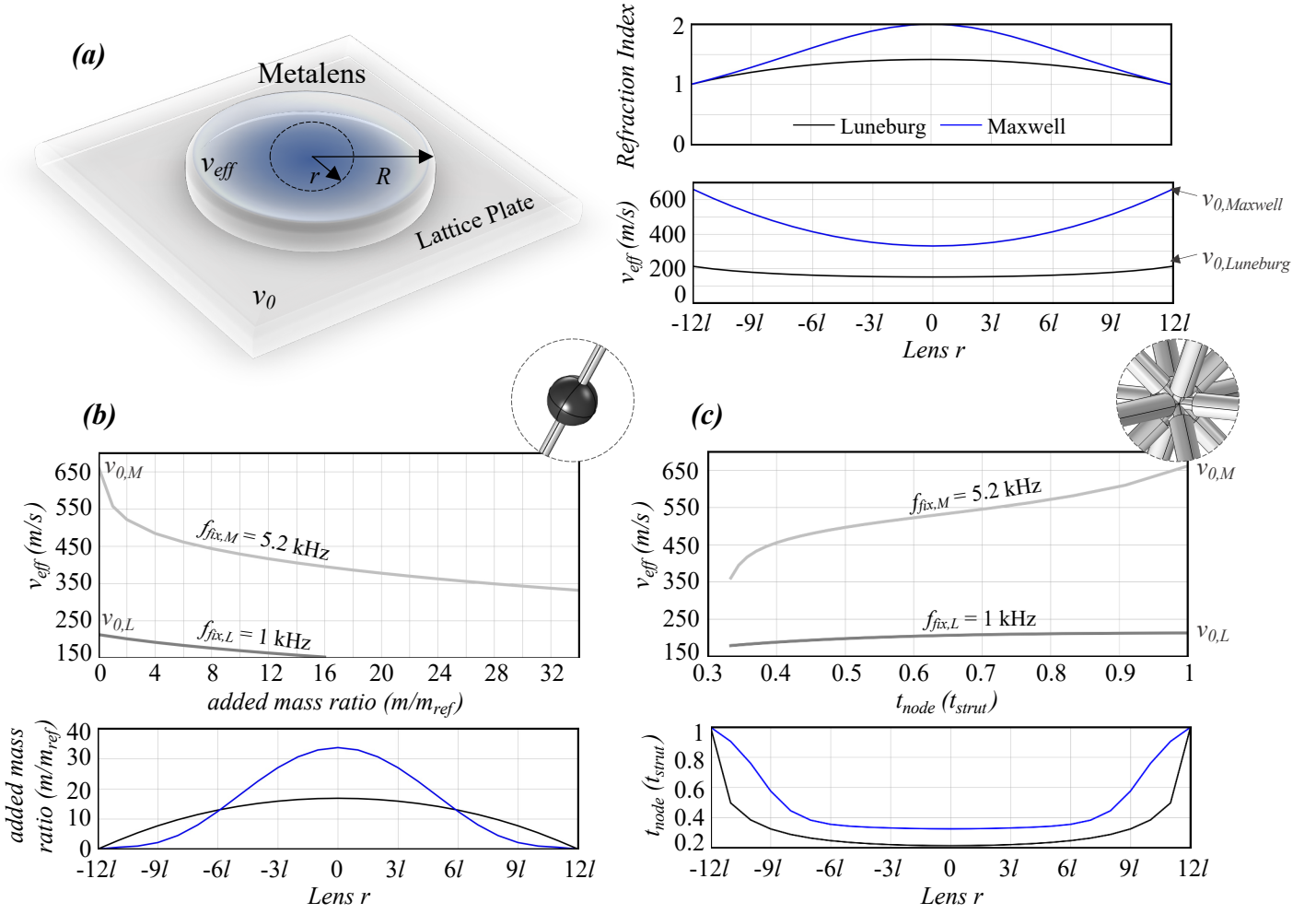


Figure 6. GRIN lenses design. (a) Schematic of the metalenses setup with geometry ($R=0.72\text{m}$) and phase velocities in the lattice plate, v_0 , and metadvice, v_{eff} , respectively emphasized. The right insert illustrates the index and effective velocity profiles of Luneburg (black) and Maxwell (blue) lenses as a function of the radial coordinate, r . $v_{0,Luneburg}$ and $v_{0,Maxwell}$ are the reference velocities of waves in the base lattice plate at 1 kHz and 5.2 kHz. At $r=R$, $v_{eff} = v_0$. (b) and (c) Design parameters of GRIN lenses comprising the customized octets with auxiliary masses or variable node thickness (see Figures 1c and d). The top insert represents the variation of effective phase velocity with respect to the tuning parameter at the fixed design frequencies of Luneburg and Maxwell lenses. The derived parameters are reported in the bottom inset.

speed-up of the waves that propagate from hinge-based ($t_{node} = 0.3 t_{strut}$) to stiffer lattices ($t_{node} = t_{strut}$). These findings serve as a bridge between the theoretical profiles of GRIN lenses and their actual implementation using reticulated structures, as they relate the octet properties to the refractive index, n , by means of the effective velocity.

After computing the refractive index profiles of the Luneburg and Maxwell lenses with the formula from Equation 2, as shown in Figure 6a for increasing radial coordinate, the following expression for the refractive index,

$$n(r) = \frac{v_0}{v_{eff}}, \quad (3)$$

is used to retrieve the phase velocity distributions illustrated in the bottom inset of Figure 6a. Finally, an inverse design approach, relying on the relations in top Figures 6b and c, is adopted to identify the tuning parameters of the customized octets at different r , based on the input effective velocity. The designed point masses and node thicknesses are outlined in Figures 6b and c for Luneburg and Maxwell lenses. Specifically, embedded masses from $3m_{ref}$ to $17m_{ref}$ or node thicknesses ranging from 0.2 to $1 t_{strut}$ are determined according to the Luneburg lens refractive index (from 1 to 1.41). The fish-eye lens, instead, originates from a stronger variation of the index profile (from 1 to 2), which requires masses from 1 to $34m_{ref}$ or t_{node} to vary between 0.3 and $1 t_{strut}$.

These designs, engineered via Bloch theory, are validated by means of time domain numerical simulations of waves traveling in the finite plate of Figure 3a, with the Real-ESSI Simulator (see Methods). Both GRIN metalenses are obtained

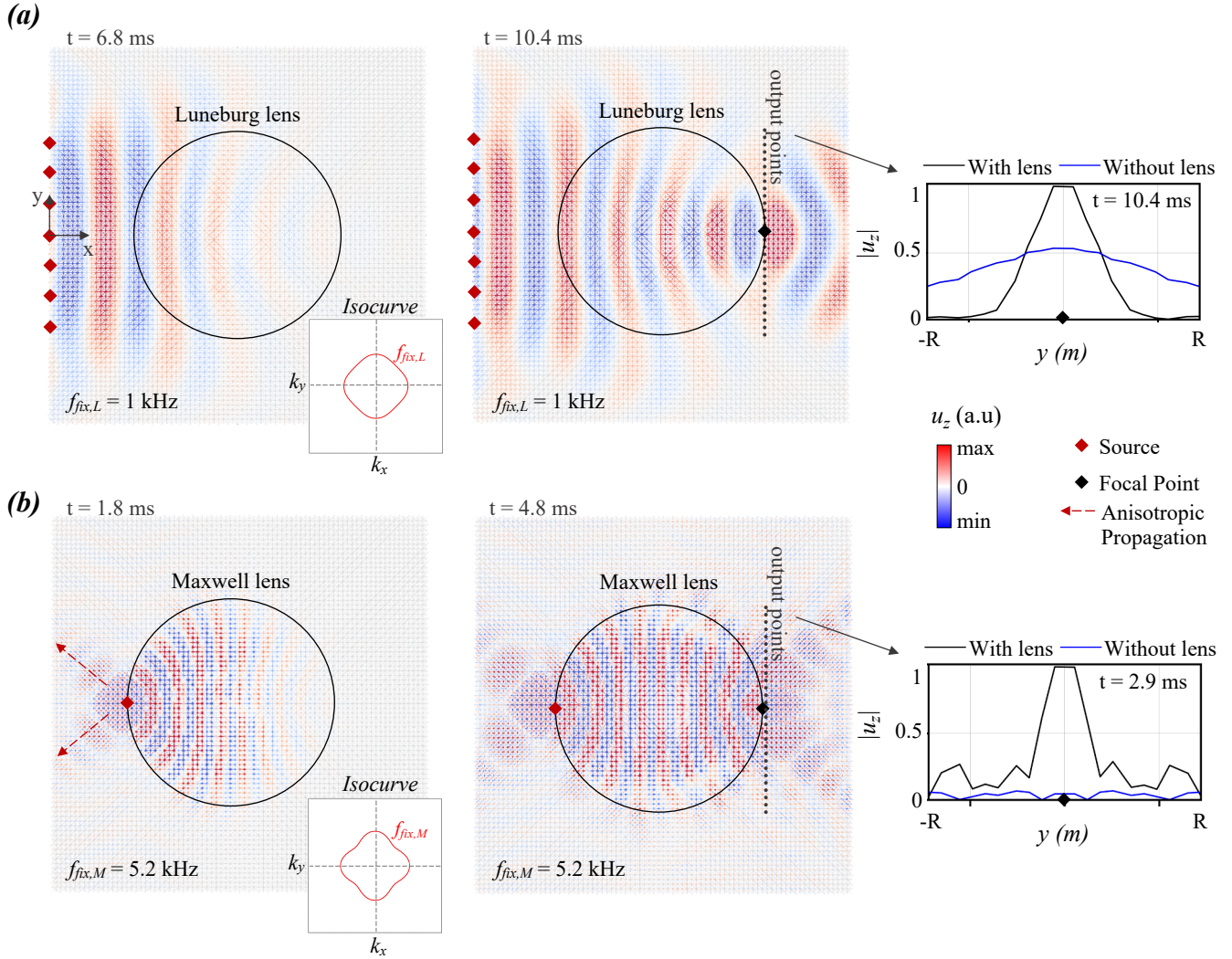


Figure 7. Wave field snapshots in gradient-index lenses consisting of octets with embedded masses. (a) Luneburg lens (black circle) with impinging plane sinusoidal wave of frequency $f_{fix,L}$ at two consecutive instants. (b) Maxwell lens excited by a point source (red diamond) of frequency $f_{fix,M}$ at two instants. In both figures, the isofrequency contours of a standard octet-based plate within the first Brillouin zone at 1 and 5.2 kHz are depicted in the bottom right insets. The flexural displacement recorded by a line of receivers is compared to the equivalent field in a bare plate (insets).

by endowing the octet cells with the masses estimated in Figure 6b and are excited by sinusoidal sources tuned at the design frequencies $f_{fix,L}$ and $f_{fix,M}$. As input signal for the Luneburg one, we use a plane wave of 40ms and 1kHz. In the Maxwell case we instead use a point-like source of frequency 5.2 kHz and duration 10ms. The wave field travels through the lenses with minimal losses and reflections, thanks to the gradual variation of properties from the plain octet lattice at $r = R$ to the center of the device that minimize the impedance mismatch (see videos in the Supplementary Material). In Figure 7a, a plane wave impinging on the left side of the Luneburg lens at 6.8 ms is progressively bent by the smooth refractive index transition and its trajectory is steered toward a diametrically opposite focal point placed on its surface ($t=10.4$ ms). An array of receivers, positioned along this edge, outlines the significant energy localization generated by the lens. A sharp spike emerges in the out-of-plane displacement u_z and its peak value is almost twice as large as its counterpart on the bare plate.

Similarly, two distinct time instants in Figure 7b validate the Maxwell lens design, where the wave originating from a point source located at the leftmost side of the lens is guided toward an antipodal focus thus, creating the typical fish-eye effect. Notice that, a non-circular wavefront is produced by the fields of the source and focal point in the surrounding plate, which instead propagate along preferential directions (approximately at 45°) due to the anisotropic character of the standard octet lattice. This behavior is further corroborated by the isofrequency contours of the standard octet lattice at $f_{fix,M}$, reported in the bottom inset of Figure 7b. A 70×70 plate, complemented with absorbing boundary conditions and a broadband point source placed at its center, is leveraged for the numerical derivation of the isocurves. The resulting wave field is spatio-temporally

Fourier transformed and the snapshot corresponding to 5.2 kHz is then extracted. The circular isofrequency contours, typical of an isotropic medium, distort here to a rhombic shape emphasizing the anisotropic nature of the lattice. The wave vectors impinging any of these contours are transmitted along the diagonals of the first Brillouin zone, causing the wave field in the real space to assume the cross-like form that emerges in Figure 7b. A similar anisotropic trait can be appreciated at lower frequencies ($f_{fix,L} = 1$ kHz) upon inspection of the corresponding isofrequency contour (bottom inset of Figure 7a). In addition, the anisotropy explains the near-zero vertical displacement in the receivers of the bare plate, blue curve in the inset of Figure 7b, which juxtaposes with the peak of the highly focused signal from the lens (black line). Equivalent results are obtained when the lens design is based on the variation of the node thickness. The only difference lies in the shape of the metadvice, squared instead of circular, to avoid discontinuities in the boundary conditions of the struts.

Discussion

We have demonstrated the potential of octet-based lattice plates in controlling the trajectories of asymmetric Lamb-like waves, be it via attenuation or wave guiding. Starting from the cellular architecture of this structure, we prove the standard octet unit is capable of supporting a Fano-type bandgap (3.85-5.08 kHz) induced by the coalescence of local bending resonances and Bragg frequency, opening the avenue for an easy-to-tune, single-phase material in elastic applications. The design of this woven structure is simplified by viewing the struts as Euler-Bernoulli beams clamped at both their ends and leveraging the analytical expression of the fundamental flexural mode as a prediction paradigm for the bandgap opening frequency; furthermore, since the octet contains struts of length and direction identical to that of the primitive lattice vectors, it creates a medium in which the clamped-clamped fundamental resonance exists as a standing wave between nodes, hence it is a medium in which local bending resonances and Bragg frequencies coincide, resulting in destructive interferences and a broadband resonant based bandgap.

The two tuning parameters extrapolated from this analogy, midpoint added masses and joint thickness, are proven to control the frequency content of the attenuation zone as well as the slope of the low and high-frequency bands exhibiting out-of-plane polarization. The opening frequency of the bandgap is inversely correlated with the masses and directly correlated with the node thickness; heavier masses drive the forbidden range to lower frequencies and reduce the phase velocity of waves in the lattice, conversely, thicker nodes shift the content of the attenuation zone to higher values and privilege the transmission of faster waves.

Drawing from these intrinsic dynamic behaviors, four devices for controlling ray trajectories are successfully engineered. The devices operate over a range of scales, the metabarriers leverage the bandgap and hence operate within a Bragg-scattering regime; on the other hand, the Luneburg lens is based on spatial variations of the low-frequency A_0 mode and hence the underlying octet cells behave in a subwavelength manner.

The constant metabarrier confirms the existence of a hybridization bandgap (1.8-2.8 kHz) stemming from the interaction between the propagating flexural field and octet units equipped with auxiliary masses. The wave impinging the resonant members is backscattered and prevented from being transmitted within the metastructure. Whilst the bandwidth of the constant metabarrier is broad, the bandgap and frequency range is spatially localized; we introduce a graded design capable of, not only tripling the mitigation width (1.14-5.1 kHz), but also spatially filtering the spectrum via a rainbow trapping mechanism, amplifying a large spectrum of frequencies within its resonating struts. The generating mechanism of the stop band, initially exploited by the lattice metabarriers to match the frequency content of incoming fields and inhibit them, serves to also tune the phase velocity within a bounded region and enable wave steering. Two GRIN lenses, the Luneburg and Maxwell fish-eye, are successfully implemented by gradually adjusting the properties of the customized octets according to the theoretical index spatial distribution, thus paving the way for novel applications of this face-centered cubic topology in wave focusing.

Although the dynamic assessment of three-dimensional woven lattices is still at a primordial stage compared to the existing knowledge on their static mechanical properties, the outcomes of our work have shed light on the hidden potential of the octet and tuning parameters. The ease of scaling to different wavelengths that characterizes this structure renders it even more attractive for applications in a variety of domains, including vibration isolation or conversion of focused energy. Indeed, the vibration energy trapped and focused, respectively by the struts and metalenses, could be harvested and converted into other forms of energy, e.g., electrical, by attaching piezoelectric components to the lattice. Future steps could, for instance, address the complicated matter of stress concentration due to dynamic loading, as well as the experimental validation of the proposed structures or the extension to different lattice unit cell based both on struts and sheets such as foams.

Methods

Bloch Analysis. The dispersion relation, reported in Figure 2a (red dotted line), is solved using the finite element method, performed by the software COMSOL Multiphysics[®], by sweeping through the required wavevector \mathbf{k} determining the permitted frequencies $\omega = \omega(\mathbf{k})$ as an eigenvalue and the displacement field as an eigenvector. Our choice of fundamental cell (Figure 1a) is a conventional cubic-like unit cell over a primitive one¹⁵, which allows us to align the base vectors with the propagation

direction of interest. This makes the comparison between the band structure stemming from the FFT analysis performed on the time-transient finite lattice section (Figure 1b) and the eigenmodal analysis straightforward as we only know the displacement fields along the beams and not everywhere in the cell. With this choice of unit cell the ends of the struts either correspond to a node point or lie on the edges of the cell, we apply either continuity conditions or quasi-periodic Bloch conditions at the strut ends as appropriate; hence the displacement field takes the following well known form:

$$\mathbf{u}(\mathbf{x}) = \mathbf{U}(\mathbf{x})e^{2\pi i(\mathbf{k}\cdot\mathbf{x} - \omega t)}, \quad (4)$$

where $\mathbf{k} = \kappa_x \mathbf{e}_x + \kappa_y \mathbf{e}_y + 0\mathbf{e}_z$ denotes the in-plane Bloch wavevector, ω the frequency assuming harmonic time-dependence and $\mathbf{U}(\mathbf{x})$ is a periodic function satisfying:

$$\mathbf{U}(\mathbf{x} + n\mathbf{a}_1 + m\mathbf{a}_2) = \mathbf{U}(\mathbf{x}), \quad (5)$$

for any integers n and m . We restrict our attention to waves propagating along the x -axis, hence consider only \mathbf{k} along the Γ - X portion of the irreducible Brillouin zone ($0 - \frac{1}{2l} 1/m$). The struts are modeled as EB beams with 6 degrees of freedom in each node (inset in Figure 1a), reducing the high computational cost of the simulations that would arise when using solid elements. The EB theory was selected over Timoshenko theory upon fulfilling the condition $EI/0.88AGl_{strut}^2 \ll 1$, with A and I area and moment of inertia and G shear modulus, as the slenderness of the beams makes shear deformations negligible.

Time-transient Simulations. The black portion in the band structure (Figure 2a) stems from time-transient simulations of waves propagating in the finite plate shown in Figure 1b, by means of the finite element software Real-ESSI Simulator⁵⁹. The system is excited by a modulated plane sweep source ranging from 0.1 to 9 kHz with components in all three directions of the space. The asymmetric Lamb waves propagating in the plate are recorded by an array of points lying perpendicularly to the source along the metabarrier center (blue dotted line in Figure 1b) and the resulting wave field u_z is spatio-temporally Fourier transformed to derive the correspondent band structure.

The metadevices (Figure 3) are tested via 3D time-transient analyses conducted with the parallel version of the Real-ESSI Simulator⁵⁹ in order to substantially reduce the computational time. The Newmark integration method is employed with γ equal to 0.505. The parameter γ controls the numerical or algorithmic damping, that is inserted into the model to damp out any non-realistic high frequencies stemming from model discretization (γ equal to 0.5 would correspond to zero numerical damping). It should be noted, here, that this type of damping cannot be used to represent any physical damping mechanism (e.g. viscous damping, hysteretic damping), while improper use could lead to unrealistic attenuation of the real response of the model⁶⁰ (i.e. values greater than 0.5 should be used with caution). External software are employed for both pre- and post-processing. Specifically, the geometry and mesh (Figure 3a) are generated with the 3D finite element generator Gmsh and a translator, called gmESSI, is invoked to convert the mesh file from Gmsh to a format readable by Real-ESSI. The mesh of the struts in the lattice consists of three-dimensional EB beam elements. The customized cells in Figures 1c and d can be easily implemented either by adding point masses to the center of the struts or locally modifying their cross-section in the node area, condensing the degree of complexity to the design stage with Gmsh. Although the Real-ESSI Simulator output results can be visualized with the open-source application Paraview after loading the PVESSIReader plugin⁵⁹, for this study an in-house code, written in Python, was employed to postprocess and later visualize the wave field in Paraview.

The in-plane size of the full frame plate is specified by the number of cells, $N_{cells,x}$ and $N_{cells,y}$ in Figure 3a, multiplied by the cell width, l . This domain is tested under vertically polarised excitations with unit amplitude that entail flexural Lamb waves propagating along x . Depending on the assessed metastructure, the input may be a line, for metabarriers and Luneburg lens, or punctual source, for Maxwell lens, and its frequency content span from that of a pulse-like Ricker excitation to a monochromatic source (inset of Figure 3a). Absorbing layers using quadratically increasing Rayleigh damping (ALID)⁵³, defined along the five outer cell arrays of the plate, are implemented to mimic an unbounded domain thus, minimizing undesirable reflections from the boundaries. A total of twenty absorbing layers on every edge is considered, each of thickness $l/4$, and a mass proportional damping with maximum coefficient c_{max} equal to $2 \cdot 10^4$ is assumed. The inner portion of the plate is, instead, left damping-free to avoid compromising the resonance of the struts and given that the selected material, versatile plastic, is characterized by a low quality factor ($Q=50$).

References

1. Gibson, L. J. & Ashby, M. F. *Cellular Solids: Structure and Properties* (Cambridge University Press, Cambridge, 1997).
2. Maconachie, T. *et al.* SLM lattice structures: Properties, performance, applications and challenges. *Mater. & Des.* **183**, 108137 (2019).
3. Phani, A. S., Woodhouse, J. & Fleck, N. Wave propagation in two-dimensional periodic lattices. *The J. Acoust. Soc. Am.* **119**, 1995–2005 (2006).

4. Brillouin, L. *Wave propagation in periodic structures: electric filters and crystal lattices*, vol. 2 (Dover publications, 1953).
5. Simon, S. H. *The Oxford solid state basics* (Oxford University Press, Oxford, UK, 2013).
6. Delpero, T., Schoenwald, S., Zemp, A. & Bergamini, A. Structural engineering of three-dimensional phononic crystals. *J. Sound Vib.* **363**, 156–165 (2016).
7. Kaina, N., Fink, M. & Lerosey, G. Composite media mixing bragg and local resonances for highly attenuating and broad bandgaps. *Sci. reports* **3**, 1–7 (2013).
8. Taubert, R., Dregely, D., Stroucken, T., Christ, A. & Giessen, H. Octave-wide photonic band gap in three-dimensional plasmonic bragg structures and limitations of radiative coupling. *Nat. communications* **3**, 1–6 (2012).
9. Goldberg, D. *et al.* Exciton-lattice polaritons in multiple-quantum-well-based photonic crystals. *Nat. Photonics* **3**, 662–666 (2009).
10. Gonella, S., To, A. C. & Liu, W. K. Interplay between phononic bandgaps and piezoelectric microstructures for energy harvesting. *J. Mech. Phys. Solids* **57**, 621–633 (2009).
11. Liebold-Ribeiro, Y. & Körner, C. Phononic band gaps in periodic cellular materials. *Adv. Eng. Mater.* **16**, 328–334 (2014).
12. Junyi, L. & Balint, D. A parametric study of the mechanical and dispersion properties of cubic lattice structures. *Int. J. Solids Struct.* **91**, 55–71 (2016).
13. Li, Y., Baker, E., Reissman, T., Sun, C. & Liu, W. K. Design of mechanical metamaterials for simultaneous vibration isolation and energy harvesting. *Appl. Phys. Lett.* **111**, 251903 (2017).
14. An, X., Lai, C., Fan, H. & Zhang, C. 3D acoustic metamaterial-based mechanical metalattice structures for low-frequency and broadband vibration attenuation. *Int. J. Solids Struct.* **191**, 293–306 (2020).
15. Ashcroft, N. W. & Mermin, N. D. *Solid State Physics* (Holt-Saunders, 1976).
16. Deshpande, V. S., Fleck, N. A. & Ashby, M. F. Effective properties of the octet-truss lattice material. *J. Mech. Phys. Solids* **49**, 1747–1769 (2001).
17. Ashby, M. F. Cellular solids—scaling of properties. *Cell. Ceram. Struct. Manuf. Prop. Appl.* 1–17 (2005).
18. Arya, M. & Steeves, C. A. Bandgaps in octet truss lattices. In *Proceedings of the 23rd Canadian Congress on Applied Mechanics*, 471–474 (Vancouver, Canada, 2011).
19. Gerard, N. J. *et al.* Three-dimensional trampolinelike behavior in an ultralight elastic metamaterial. *Phys. Rev. Appl.* **16**, 024015 (2021).
20. Chen, Y. & Wang, L. Periodic co-continuous acoustic metamaterials with overlapping locally resonant and Bragg band gaps. *Appl. Phys. Lett.* **105**, 191907 (2014).
21. Arretche, I. & Matlack, K. H. On the interrelationship between static and vibration mitigation properties of architected metastructures. *Front. Mater.* **5**, 68 (2018).
22. Lamb, H. On waves in an elastic plate. *Proc. Royal Soc. London. Ser. A, Containing papers a mathematical physical character* **93**, 114–128 (1917).
23. Graff, K. F. *Wave Motion in Elastic Solids* (Courier Corporation, 2012).
24. Colombi, A., Colquitt, D., Roux, P., Guenneau, S. & Craster, R. V. A seismic metamaterial: The resonant metawedge. *Sci. reports* **6**, 1–6 (2016).
25. Rupin, M., Lemoult, F., Lerosey, G. & Roux, P. Experimental demonstration of ordered and disordered multiresonant metamaterials for lamb waves. *Phys. review letters* **112**, 234301 (2014).
26. Colombi, A. *et al.* Elastic wave control beyond band-gaps: shaping the flow of waves in plates and half-spaces with subwavelength resonant rods. *Front. Mech. Eng.* **3**, 10 (2017).
27. Tsakmakidis, K. L., Boardman, A. D. & Hess, O. ‘Trapped rainbow’ storage of light in metamaterials. *Nature* **450**, 397–401 (2007).
28. De Ponti, J. M. *et al.* Graded elastic metasurface for enhanced energy harvesting. *New J. Phys.* **22**, 013013 (2020).
29. Liu, Y., Sun, X.-Z., Jiang, W.-Z. & Gu, Y. Tuning of bandgap structures in three-dimensional Kagome-sphere lattice. *J. Vib. Acoust.* **136** (2014).
30. Maxwell, J. Solutions of problems (prob. 3, vol. viii. p. 188). *The Camb. Dublin Math. J.* **9**, 9–11 (1854).
31. Luneburg, R. K. *Mathematical Theory of Optics* (Providence, Rhode Island: Brown University, 1944).

32. Climente, A., Torrent, D. & Sánchez-Dehesa, J. Gradient index lenses for flexural waves based on thickness variations. *Appl. Phys. Lett.* **105**, 064101 (2014).
33. Tol, S., Degertekin, F. & Erturk, A. Phononic crystal Luneburg lens for omnidirectional elastic wave focusing and energy harvesting. *Appl. Phys. Lett.* **111**, 013503 (2017).
34. Lee, D., Cho, C., Mun, J., Park, N. & Rho, J. Demonstration of steering acoustic waves by generalized Eaton lens. *Appl. Phys. Lett.* **113**, 161904 (2018).
35. Park, C. M. & Lee, S. H. Acoustic luneburg lens using orifice-type metamaterial unit cells. *Appl. physics letters* **112**, 074101 (2018).
36. Colombi, A. Resonant metalenses for flexural waves in plates. *The J. Acoust. Soc. Am.* **140**, EL423 (2016).
37. Zhu, R. *et al.* Bifunctional acoustic metamaterial lens designed with coordinate transformation. *Appl. Phys. Lett.* **110**, 113503 (2017).
38. Fuentes-Domínguez, R. *et al.* Design of a resonant Luneburg lens for surface acoustic waves. *Ultrasonics* **111**, 106306 (2021).
39. Colombi, A., Guenneau, S., Roux, P. & Craster, R. V. Transformation seismology: composite soil lenses for steering surface elastic Rayleigh waves. *Sci. reports* **6**, 1–9 (2016).
40. Ruzzene, M., Scarpa, F. & Soranna, F. Wave beaming effects in two-dimensional cellular structures. *Smart materials structures* **12**, 363 (2003).
41. Casadei, F. & Rimoli, J. Anisotropy-induced broadband stress wave steering in periodic lattices. *Int. J. Solids Struct.* **50**, 1402–1414 (2013).
42. Pal, R. K., Rimoli, J. & Ruzzene, M. Effect of large deformation pre-loads on the wave properties of hexagonal lattices. *Smart Mater. Struct.* **25**, 054010 (2016).
43. Zelhofer, A. J. & Kochmann, D. M. On acoustic wave beaming in two-dimensional structural lattices. *Int. J. Solids Struct.* **115**, 248–269 (2017).
44. Xie, Y. *et al.* Acoustic imaging with metamaterial Luneburg lenses. *Sci. reports* **8**, 1–6 (2018).
45. Zhao, L. *et al.* Ultrasound beam steering with flattened acoustic metamaterial Luneburg lens. *Appl. Phys. Lett.* **116**, 071902 (2020).
46. Bayat, A. & Gaitanaros, S. Wave directionality in three-dimensional periodic lattices. *J. Appl. Mech.* **85**, 011004 (2018).
47. Pennec, Y., Djafari-Rouhani, B., Larabi, H., Vasseur, J. & Hladky-Hennion, A. Low-frequency gaps in a phononic crystal constituted of cylindrical dots deposited on a thin homogeneous plate. *Phys. Rev. B* **78**, 104105 (2008).
48. Goffaux, C. *et al.* Evidence of Fano-like interference phenomena in locally resonant materials. *Phys. review letters* **88**, 225502 (2002).
49. Wang, P., Casadei, F., Kang, S. H. & Bertoldi, K. Locally resonant band gaps in periodic beam lattices by tuning connectivity. *Phys. Rev. B* **91**, 020103 (2015).
50. Nolde, E., Craster, R. & Kaplunov, J. High frequency homogenization for structural mechanics. *J. Mech. Phys. Solids* **59**, 651–671 (2011).
51. Aguzzi, G., Colombi, A., Dertimanis, V. K. & Chatzi, E. Metamaterials for groundborne vibration absorption in pillars. In *Proceedings of ISMA2020 including USD2020*, 355 (KU Leuven, 2020).
52. Low, K. Closed-form formulas for fundamental vibration frequency of beams under off-centre load. *J. sound vibration* **201**, 528–533 (1997).
53. Rajagopal, P., Drozd, M., Skelton, E. A., Lowe, M. J. & Craster, R. V. On the use of absorbing layers to simulate the propagation of elastic waves in unbounded isotropic media using commercially available finite element packages. *Ndt & e international* **51**, 30–40 (2012).
54. Miroshnichenko, A. E., Flach, S. & Kivshar, Y. S. Fano resonances in nanoscale structures. *Rev. Mod. Phys.* **82**, 2257 (2010).
55. Lemoult, F., Kaina, N., Fink, M. & Lerosey, G. Wave propagation control at the deep subwavelength scale in metamaterials. *Nat. Phys.* **9**, 55–60 (2013).
56. Zaccherini, R. *et al.* Locally resonant metasurfaces for shear waves in granular media. *Phys. Rev. Appl.* **13**, 034055 (2020).

57. Colombi, A., Roux, P., Guenneau, S., Gueguen, P. & Craster, R. V. Forests as a natural seismic metamaterial: Rayleigh wave bandgaps induced by local resonances. *Sci. reports* **6**, 1–7 (2016).
58. Cebrecos, A. *et al.* Enhancement of sound by soft reflections in exponentially chirped crystals. *AIP Adv.* **4**, 124402 (2014).
59. B. Jeremić, G. Jie, Z. Cheng, N. Tafazzoli, P. Tasiopoulou, F. Pisanò, J. A. Abell, K. Watanabe, Y. Feng, S. K. Sinha, F. Behbehani, H. Yang, and H. Wang. *The Real-ESSI Simulator System*. University of California, Davis. (1988-2020).
60. Kanellopoulos, C., Jeremic, B., Anastasopoulos, I. & Stojadinovic, B. Use of the Domain Reduction Method to simulate the seismic response of an existing structure protected by resonating unit cell metamaterials. In *Proceedings of the XI International Conference on Structural Dynamics, EURODDYN*, 2926–2938 (2020).

Acknowledgements

GA and AC were supported by the H2020 FETOpen project BOHEME under grant agreement No. 863179 and by the Ambizione Fellowship PZ00P2-174009. CK was supported by the H2020 "INSPIRE" EU program under grant agreement No 813424. RW thanks the UK EPSRC for their support through grant EP/L016230/1.